submitted to *Geophys. J. Int.*

Supplementary materials

Wenbo Wu[1,2], Sidao Ni[1], Zhongwen Zhan[3], Shengji Wei[4,5]

[1]*State Key Laboratory of Geodesy and Earth's Dynamics, Institute of Geodesy and Geophysics, Chinese Academy of Sciences, Wuhan 430077, China. Email: sdni@whigg.ac.cn*

[2] *Department of Geosciences, Princeton University, Princeton, NJ 08541, USA.*

[3]*Seismological Laboratory, California Institute of Technology, Pasadena, CA 91125, USA.*

[4]*Earth Observatory of Singapore, Nanyang Technological University, Singapore 639798, Singapore.*

[5]*Asian School of Environment, Nanyang Technological University, Singapore 639798, Singapore.*

30 June 2018

1 SLOW CONVERGENCE OF DSM SYNTHETICS NEAR SOURCE DEPTH

Because of the near-field terms, higher angular order spherical harmonics in DSM calculation have to be involved to obtain accurate coefficients c^{lmk1}, c^{lmk2} and c^{lmk3}, as receiver depth is closer to source depth (Kawai et al. 2006). Since a point seismic source is a mathematical singularity, it is not surprising that no convergence exists at the exact position of source. However, how the convergence rate quantitatively changes with depth is unclear. More generally, this slow convergence around source depth is intrinsically problematic for all the Discrete-Wavenumber (DW) alike methods. For example, Zahradník & Moczo (1996) developed a DW-FD hybrid modeling method and used interpolation to circumvent the convergence problem of DW at source depth. Interpolation does help us avoid the singularity at the exact depth of source, but the convergence rate is still slow around the source depth, that causes significantly additional computation costs. Here, we first analyze the analytical solution of scalar Helmholtz equation in an uniform unbounded space and then numerically

investigate the oscillation behavior of DSM synthetics near source depth. We propose a solution of taking an average value over some integer periods of the oscillation to partially remove the oscillation effect and therefore save computation expanses.

1.1 Spherical harmonics expansion of the Green's function of the scalar Helmholtz equation in an uniform unbounded space

A much simplified problem, which has an analytic solution, would be greatly useful to understand the slow convergence issue. One of the best candidates would be the Green's function of the scalar Helmholtz equation in an unbounded space (see eq. 4.2 in Aki & Richards 2002),

$$\frac{\partial^2 g}{\partial t^2} = \delta(\mathbf{r_s})\delta(t) + c^2\nabla^2 g \tag{1}$$

where c is wave propagation velocity. Its time domain solution is

$$g(\mathbf{r}, t) = \frac{1}{4\pi c^2}\frac{\delta(t - |\mathbf{r} - \mathbf{r_s}|/c)}{|\mathbf{r} - \mathbf{r_s}|} \tag{2}$$

Transforming the above solution into frequency domain gives

$$g(\mathbf{r}, \omega) = \frac{e^{-i\omega|\mathbf{r}-\mathbf{r_s}|/c}}{4\pi c^2}\frac{1}{|\mathbf{r} - \mathbf{r_s}|} = \frac{-ik}{4\pi c^2}h^0_{(2)}(k|\mathbf{r} - \mathbf{r_s}|) \tag{3}$$

where $k = \frac{\omega}{c}$ is the wave number and $h^0_{(2)}$ is a second spherical Hankel function with zero order. This solution has a singularity of $\frac{1}{|\mathbf{r}-\mathbf{r_s}|}$ at the source point $\mathbf{r} = \mathbf{r_s}$. By using the properties of spherical Hankel function, the above equation is rewritten as (see the eq. 105 in the page 658 of Skudrzyk 2012)

$$\begin{aligned} g(\mathbf{r}, k) &= \frac{-ik}{4\pi c^2}h^0_{(2)}(k|\mathbf{r} - \mathbf{r_s}|) \\ &= \frac{-ik}{4\pi c^2}\sum_{l=0}^{\infty}(2l+1)\sum_{m=0}^{l}\epsilon^m\frac{(l-m)!}{(l+m)!}\cos[m(\phi - \phi_s)] \\ &\times P^{lm}(\cos(\theta_s))P^{lm}(\cos(\theta))\begin{cases} j^l(kr_s)h^l_{(2)}(kr);\ r > r_s \\ j^l(kr)h^l_{(2)}(kr_s);\ r_s > r \end{cases} \end{aligned} \tag{4}$$

where

$$\epsilon^m = 2, m > 0; \quad \epsilon^m = 1, m = 0. \tag{5}$$

$P^{lm}(\cos(\theta))$ and $P^{lm}(\cos(\theta_s))$ are the associated Legendre polynomials, where l and m indicate the angular order and azimuthal order respectively. $j^l(kr_s)$ is a spherical Bessel function and $h^l_{(2)}(kr)$ is a second spherical Hankel function.

For simplification, the source is specified on the z-axis ($\theta_s = 0.0$, $\phi_s = 0.0$), as we do in DSM calculation. Consequently, $P^{lm}(\cos(\theta_s))$ is non-zero only for $m = 0$ and the Green's function $g(\mathbf{r}, k)$ has no dependence on the azimuth ϕ. Thus, eq. (4) is simplified to

$$\begin{aligned} g(\mathbf{r},k) &= \frac{-ik}{4\pi c^2}\sum_{l=0}^{\infty}(2l+1)P^{l0}(\cos(\theta))\begin{cases} j^l(kr_s)h^l_{(2)}(kr);\ r>r_s \\ j^l(kr)h^l_{(2)}(kr_s);\ r_s>r \end{cases} \\ &= \frac{-ik}{c^2}\sum_{l=0}^{\infty}\sqrt{\frac{2l+1}{4\pi}}Y^{l0}(\cos(\theta))\begin{cases} j^l(kr_s)h^l_{(2)}(kr);\ r>r_s \\ j^l(kr)h^l_{(2)}(kr_s);\ r_s>r \end{cases} \end{aligned} \tag{6}$$

where $Y^{l0}(\cos(\theta))$ is a spherical harmonic function. Similar to the coefficients c^{lmk1}, c^{lmk2}, and c^{lmk3} in DSM, we define a coefficient

$$a^l(r,k) = \frac{-ik}{c^2}\sqrt{\frac{2l+1}{4\pi}}\begin{cases} j^l(kr_s)h^l_{(2)}(kr);\ r>r_s \\ j^l(kr)h^l_{(2)}(kr_s);\ r_s>r \end{cases} \tag{7}$$

Thus

$$g(\mathbf{r},k) = \sum_{l=0}^{\infty} a^l(r,k)Y^{l0}(\cos(\theta)) \tag{8}$$

In the following subsections, the properties, especially convergence, of a^l, are analyzed. Because of the symmetry in eq. (7), we only focus on the case $r_s > r$ in the following subsections.

1.1.1 Very low frequency

For the case of very low frequency or small wave number ($kr \ll 0$ and $kr_s \ll 0$), $j^l(kr)$ and $h^l_{(2)}(kr_s)$ have asymptotic forms (see the eqs. 9.1.7 and 9.1.9 in page 360, and the eqs. 6.1.8 and 6.1.12 in page 255 of Abramowitz & Stegun 1964)

$$\lim_{kr\to 0} j^l(kr) = \lim_{kr\to 0}\sqrt{\frac{\pi}{2kr}}J^{l+\frac{1}{2}}(kr) = \frac{2^l l!}{(2l+1)!}(kr)^l \tag{9}$$

$$\lim_{kr_s\to 0} h^l_{(2)}(kr_s) = \lim_{kr_s\to 0}\sqrt{\frac{\pi}{2kr_s}}[J^{l+\frac{1}{2}}(kr_s) - iY^{l+\frac{1}{2}}(kr_s)] = i\frac{(2l)!}{2^l l!}\frac{1}{(kr_s)^{l+1}} \tag{10}$$

Substituting the above two equations into eq. (7) gives

$$a^l(r,k) = \frac{1}{2r_s c^2\sqrt{\pi}}\frac{1}{\sqrt{(2l+1)}}(\frac{r}{r_s})^l \tag{11}$$

Because of $\frac{r}{r_s} < 1$, the coefficient a^l monotonically decreases with l and converges to zero with a rate of $\sqrt{\frac{1}{2l+1}}(\frac{r}{r_s})^l$, for given r and k. For example, $\frac{a^l|_{l=20000}}{a^l|_{l=0}} = 1.13\times 10^{-16}$ is tiny and numerically negligible, when $r_s = 6371\ km$ and $r = 6361\ km$. But for the extreme case $r = r_s$, the convergence rate is as low as $\sqrt{\frac{1}{2l+1}}$ and $\frac{a^l|_{l=20000}}{a^l|_{l=0}} = 0.005$. Thus, the convergence rate greatly depends on the ratio $\frac{r}{r_s}$.

For the worst case $r = r_s$, substituting eq. (11) into eq. (8) leads to

$$g(\mathbf{r},k) = \frac{1}{4\pi r c^2}\sum_{l=0}^{\infty} P^{l0}(\cos(\theta)) \tag{12}$$

If θ also equals $\theta_s = 0°$, the associated Legendre polynomials $P^{l0}(\cos(\theta))$ have a constant value of 1.0 and therefore the term $\sum_{l=0}^{\infty} P^{l0}(\cos(\theta))$ is not convergent at all. This makes mathematical sense, considering the source point is an intrinsic singularity in the governing eq. (1). A next question is how eq. (12) behaves for $r = r_s$ and $\theta \neq \theta_s$.

Given $r = r_s$, Fig. S1 shows the cumulative sums in eq. (12) for $\theta = 3.0°$ and $30°$. Both cumulative sums start from zero, gradually approach the levels of their theoretical values $g(\mathbf{r},k) = \frac{1}{r\cos(\theta)}$ and finally oscillate around them. However, the dominant period of the oscillation for $\theta = 3.0°$ is $\triangle l \approx 120$, larger by a factor of 10 than $\triangle l \approx 12$ for $\theta = 30°$.

For large angular order l, the associated Legendre function $P^{l0}(\cos(\theta))$ can be approximated as (see the eq. 8.721 in page 1003 of Abramowitz & Stegun 1964)

$$P^{l0}(\cos(\theta)) = \sqrt{\frac{2}{\pi l\sin(\theta)}}\cos[(l+\frac{1}{2})\theta - \frac{\pi}{4}] + O(l^{-\frac{3}{2}}) \tag{13}$$

The first term on the right hand side of the above equation is an oscillation, which decays as $\frac{1}{\sqrt{l}}$. The dominant period of the cosine oscillation is $\triangle l = \frac{360°}{\theta}$, which perfectly matches the results in Fig. S1.

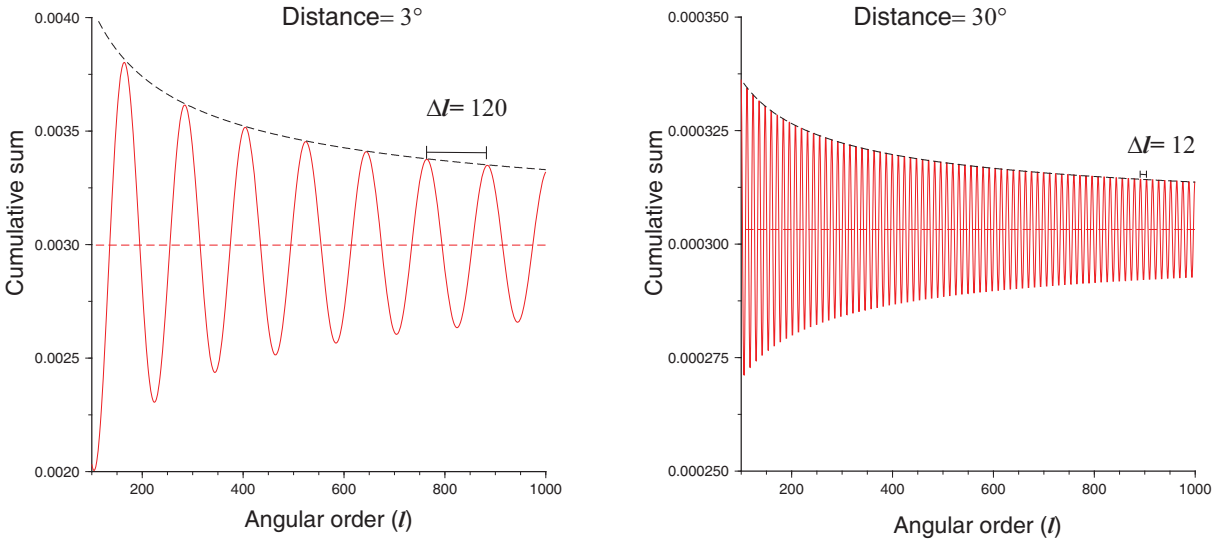

Figure S1: Cumulative sums on the right rand side of eq. 12, for a distance of 3° (red line in the left figure) and 30° (red line in the right figure). For simplicity, we assume $4\pi c^2 = 1$. Thus, the theoretical value of $g(r,k)$ equals $\frac{1}{|\mathbf{r}-\mathbf{r_s}|} = \frac{1}{r\cos(\theta)}$ (red dashed lines), where $r = r_s = 6371\ km$ and θ is the distance. The oscillations of solutions are modulated by a amplitude decay factor $\frac{1}{\sqrt{l}}$ (black dashed lines) and the period of the oscillation is inversely proportional to their distances.

1.1.2 Large angular order l

For a large angular order l (see the eq. 9.3.1 in page 365 of Abramowitz & Stegun 1964),

$$\lim_{l\to\infty} j^l(kr) = \lim_{l\to\infty}\sqrt{\frac{\pi}{2kr}}J^{l+\frac{1}{2}}(kr) = \frac{1}{\sqrt{2kr(2l+1)}}(\frac{ekr}{2l+1})^{l+\frac{1}{2}} \tag{14}$$

$$\lim_{l\to\infty} h^l_{(2)}(kr_s) = \lim_{l\to\infty}\sqrt{\frac{\pi}{2kr_s}}[J^{l+\frac{1}{2}}(kr_s) - iY^{l+\frac{1}{2}}(kr_s)] = i\sqrt{\frac{2}{kr_s(2l+1)}}(\frac{ekr_s}{2l+1})^{-l-\frac{1}{2}} \tag{15}$$

where $J^{l+\frac{1}{2}}(kr)$ and $Y^{l+\frac{1}{2}}(kr)$ are the first and second Bessel functions respectively. Substituting the above two equations into eq. (7) gives

$$a^l(r,k) = \frac{1}{2c^2 r_s\sqrt{\pi}}\frac{1}{\sqrt{2l+1}}(\frac{r}{r_s})^l \tag{16}$$

Comparing eq. (16) to eq. (11), they are exactly the same. Thus, the conclusions, regarding the convergence rate and oscillation behavior stated in subsection 1.1.1, are also valid here for any frequency, as long as the angular order l is sufficiently large.

Further more, it turns out that the turning point l_t, above which the validity of asymptotic forms eqs. (14) and (15) builds up, is $l + \frac{1}{2} = kr$. This equation is just the well-known relationship between the parameters of wavenumber and angular order. The physical interpretation behind l_t is that any non-decay waves should have a phase velocity faster than c_t.

1.2 Slow convergence of DSM synthetics around source depth

As shown in the eq. (1) of the main text, DSM synthetic $\mathbf{u}(r, \theta, \phi)$ of each frequency is expressed as an infinite sum ($l \to +\infty$) of weighted spherical harmonics. In practice, the sum is truncated at a sufficiently large angular order, where the amplitude of expansion coefficients $(\sum_m [|c^{lmk1}|^2 + |c^{lmk2}|^2 + |c^{lmk3}|^2])^{1/2}$ decays below a given tiny fraction (e.g. 0.001%) of the maximum amplitude. Kawai et al. (2006) found that synthetic becomes rapidly accurate, once the involved maximum angular order is larger than a critical threshold angular order l_d.

However, the specific number of the critical threshold angular order l_d greatly depends on the depth of source. Given a receiver on the free surface of the Earth, a shallower source requires a higher critical threshold angular order l_d to obtain accurate synthetic, due to the near-field terms (Kawai et al. 2006). Suppose that there is a source buried at a depth of 10 km and two teleseismic stations are placed at a distance of $\theta = 30°$, but different depths. Fig. S2 shows the vertical component synthetics of the two stations for a period of 100 s. Both cumulative sums of the real parts of the solutions oscillate, when l is larger than the threshold angular order of $l_t = 97$, and finally converge to a similar value. These two stations have the same oscillation period $\triangle l = 12$ (insets in Fig. S2), that indicates a depth independence. However, the convergence rate of the deeper receiver is much faster than the shallower one. The amplitudes of the oscillations for both stations decay with increasing l, which are well approximated by a form of $\frac{1}{\sqrt{2l+1}}(\frac{r}{r_s})^l$. This decay factor or convergence rate greatly depends on the ratio $\frac{r}{r_s}$, that explains the slow convergence of synthetics around source depth. This decay form is also reflected in the change of expansion coefficient amplitude with the radius

r. For given l and r_s, the amplitude of the expansion coefficient c^{lmk1} decays as a power function $(\frac{r}{r_s})^l$ for $r_s > r$ and $(\frac{r_s}{r})^l$ for $r_s < r$ (Fig. S3). For example, the amplitude ratio of $c^{lmk1}|_{l=12000}$ to $c^{lmk1}|_{l=4000}$ is larger than 0.1 at the source depth, but decays to $< 10^{-5}$ at the depth either 10 km shallower or 10 km deeper than the source.

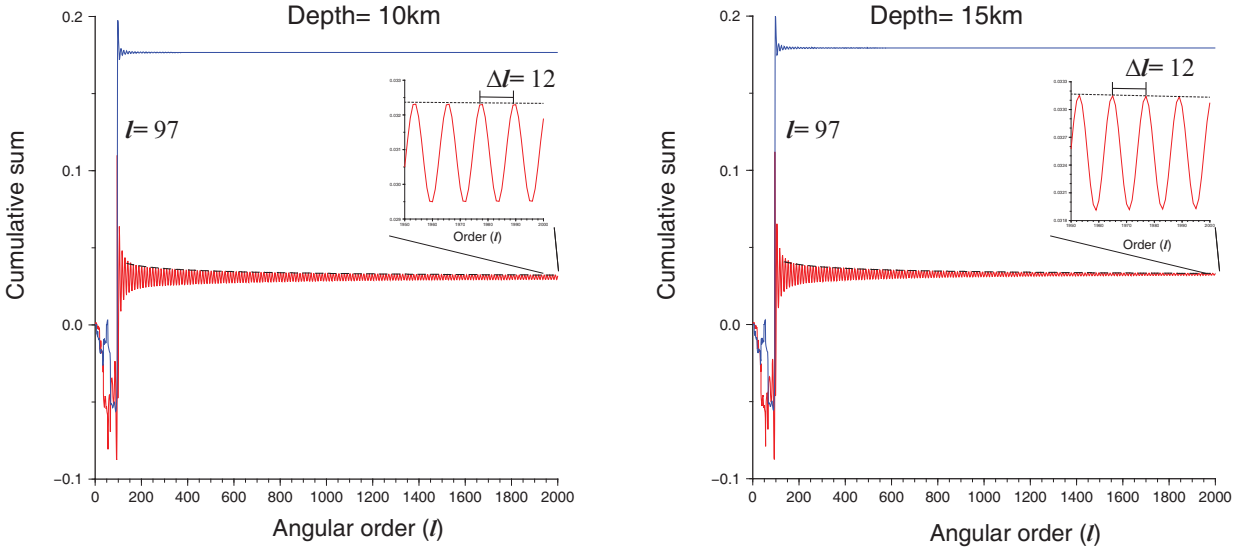

Figure S2: Oscillation behavior of DSM synthetic u_r (period T = 100 s) at large angular orders. An explosion source at a depth of 10 km is modeled and two teleseismic receivers are located at the same horizontal distance of 30°, but different depths (10 km in the left figure and 15 km in the right figure). The blue lines are imaginary parts and the red lines show real parts. The black dashed lines indicate $\frac{1}{\sqrt{2l+1}}(\frac{r}{r_s})^l$ decay shapes. The cumulative sums of real parts oscillate with a period of $\triangle l = 12$ (zoom-in insets), once they pass the threshold angular order $l_t = 97$.

The slow convergence and oscillation behavior are consistent with the conclusions stated in Section 1.1, although some minor differences exist, due to the more complex 1D Earth structure here than the homogeneous unbounded space used in Section 1.1. For example, $\triangle l = 12$ is exactly equal to $360°/\theta$, where $\theta = 30°$ is the distance. The rough decay rate $\frac{1}{\sqrt{2l+1}}(\frac{r}{r_s})^l$ is also consistent with the conclusion in section 1.1. The threshold angular order $l_t = 97$ in Fig. S2 corresponds to a phase velocity of $c_t = 2\pi r/[T(l_t + 1/2)] = 4.11\ km/s$. This phase velocity is between the S-wave velocity 3.36 km/s and P-wave velocity 5.8 km/s

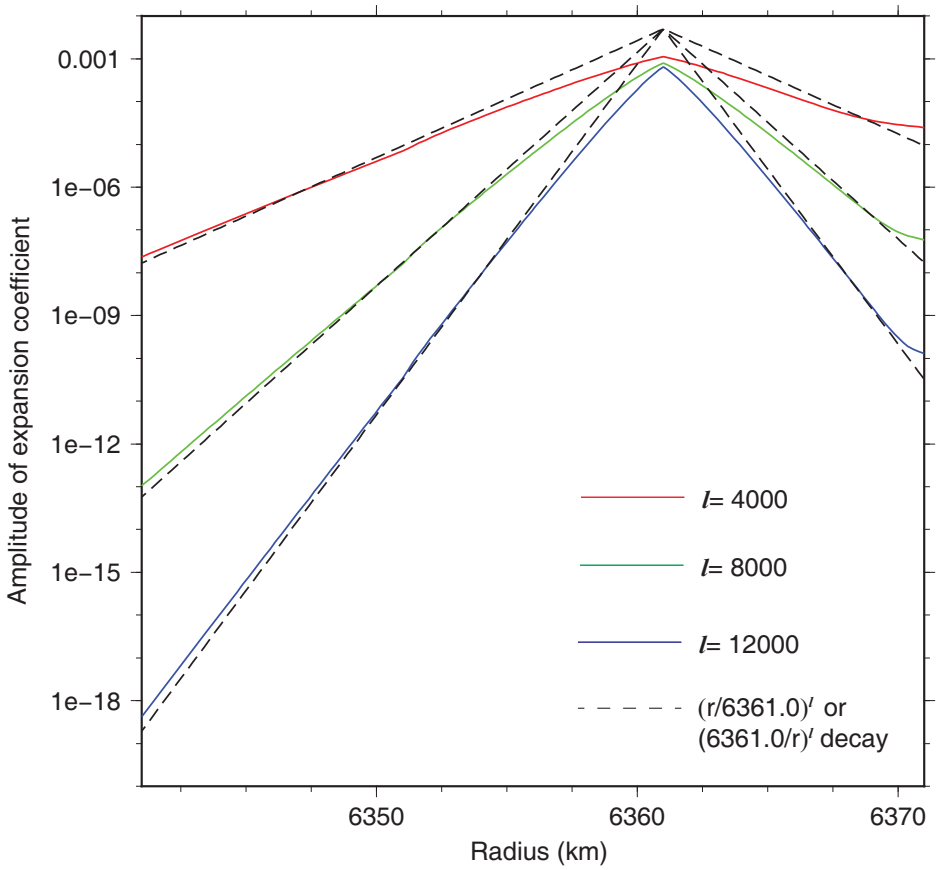

Figure S3: Amplitude of the expansion coefficient c^{lmk1} (period T = 100 s), as a function of radius. An explosion source is placed at a radius of 6361 km, the same as Fig. S2. The dashed lines indicate the power function decay trends, which fit the data well on both sides of the source radius. The amplitude changes are disturbed around the discontinuities of seismic properties, such as the free surface and middle crust interface at a depth of 20 km.

in the upper crust and very close to the phase velocity of surface wave with a period of 100 s.

Fig. S4 and S5 show the results for a point source of vertical single force at a depth of 0 km, which are the Green's functions used in our hybrid method. These results are similar to the explosion source (Fig. S2 and S3). For example, both of them show oscillation behavior at $l > 97$ and the oscillation period is $\triangle l = 12$ (Fig. S2 and S4). The amplitude of the expansion coefficient decays as a power function $(\frac{r}{r_s})^l$ or $(\frac{r_s}{r})^l$ (Fig. S3 and S5). However, comparing Fig. S4 to S2, the vertical single force shows more complex amplitude changes of real parts of u_r than the explosion source. For example, for the explosion source, the

amplitudes of real parts of u_r monotonically decrease with l (Fig. S2), once l is larger than the threshold angular order $l_t = 97$. In contrast, the amplitude change is not monotonous for the single force. For the station at a depth of 10 km below the source, the amplitude shows an increasing trend with l in a range of $\sim 200 < l < \sim 900$ (red line in the right figure of Fig. S4). When the station is closer to the source (e.g. 1 km below the source), this increasing trend spans a wider range of $\sim 200 < l < \sim 2000$ *or maybe higher* (red line in the left figure of Fig. S4). We speculate that this might be due to different radiation patterns between an explosion source and a single force.

In summary, the near-field terms lead to slow convergence of DSM synthetics around source depth, that requires higher angular order harmonics involved to obtain accurate synthetics. But the near-field terms should be minor important for teleseismic synthetics (e.g distance $> 20°$), because they are expected to decay to a negligible level. The fact is that the near-field terms give rise to numerical oscillation around true values of teleseismic synthetics. Hence, our solution is taking an average value over some integer periods of oscillation to suppress the oscillation effect.

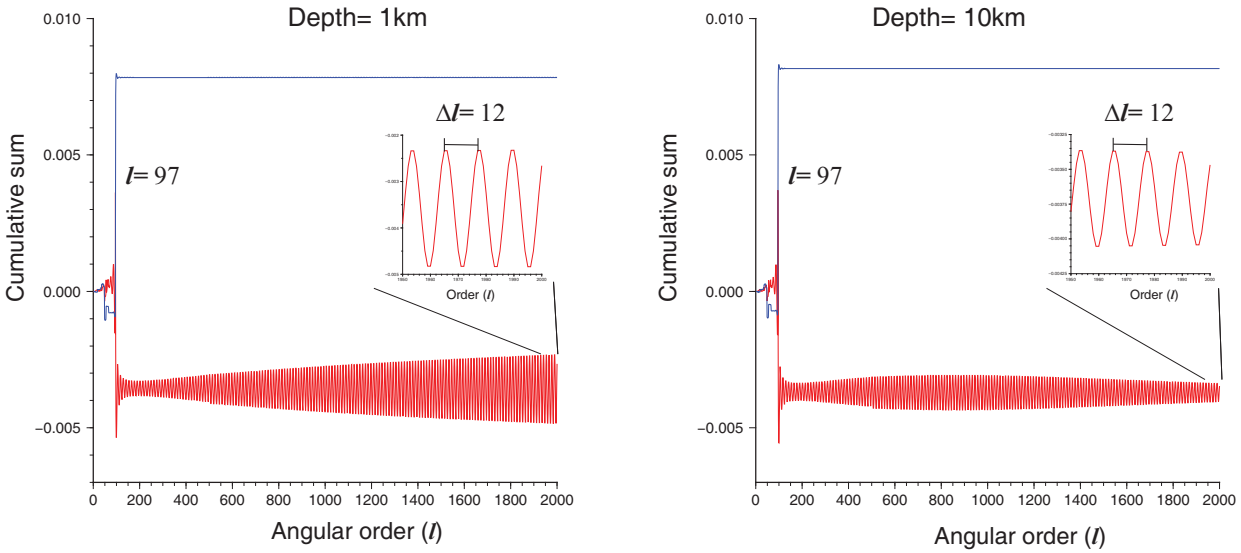

Figure S4: Same as Fig. S2, but the source is a vertical single force at a depth of 0 km and the stations have depths of 1 km (left figure) and 10 km (right figure).

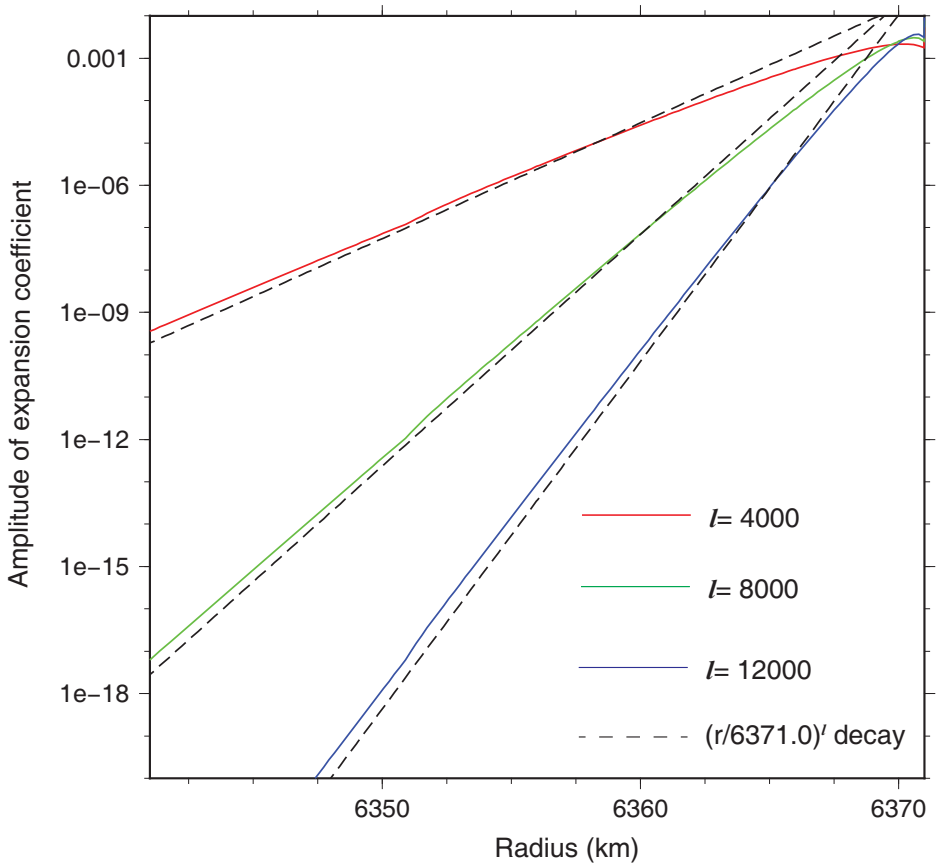

Figure S5: Same as Fig. S4, but the source is a vertical single force at a depth of 0 km.

2 LAGRANGE POLYNOMIAL INTERPOLATION OF GREEN'S FUNCTIONS

As described in the main text, an equally spaced distance table is prespecified and Green's functions associated with each distance in the table are computed and stored. The Green's functions on target distances are then obtained by Lagrange interpolations from the database. This method substantially reduces the number of Green's function records and thus the demand for storage. The quality of the Lagrange interpolation depends on the distance interval and the degree of polynomial. Generally, the distance interval should decrease with the slowness and frequency of the seismic waves, because smaller slowness and/or lower frequency seismic waves usually have smoother spatial variations with distance. For example, Fig. S6 shows displacement Green's functions in a distance range of $30.5^o - 31.5^o$ for two frequencies of 0.1 Hz and 1 Hz. The 0.1 Hz Green's functions show smoother variations with distance

than the 1 Hz results. In order to obtain accurate interpolated Green's functions, the distance space for the 1 Hz must be much smaller than the 0.1 Hz.

Fig. S7 shows the results of Lagrange polynomial interpolations with different degrees. Higher degree polynomials produce more accurate interpolation results, but take more computation time. In order to balance the computation time against accuracy, we choose 16-degree Lagrange polynomial interpolation.

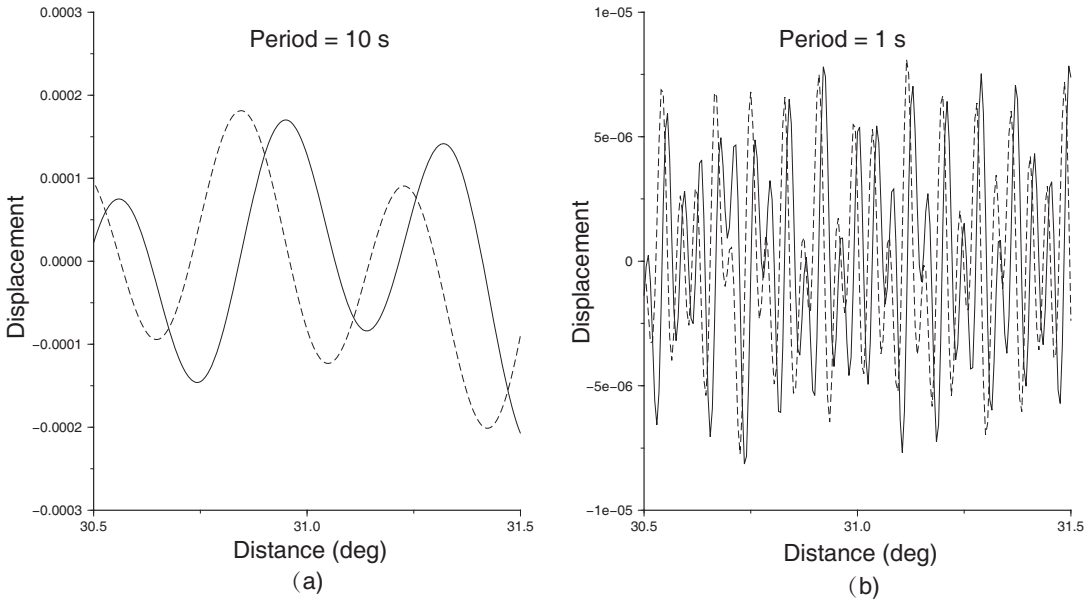

Figure S6: Complex values of vertical displacement Green's functions at a depth of 80 km. The source is a vertical single force applied on the free surface. The left figure corresponds to the frequency of 0.1 Hz and the right figure shows the 1 Hz results. The solid lines are real parts and the dashed lines show imaginary parts.

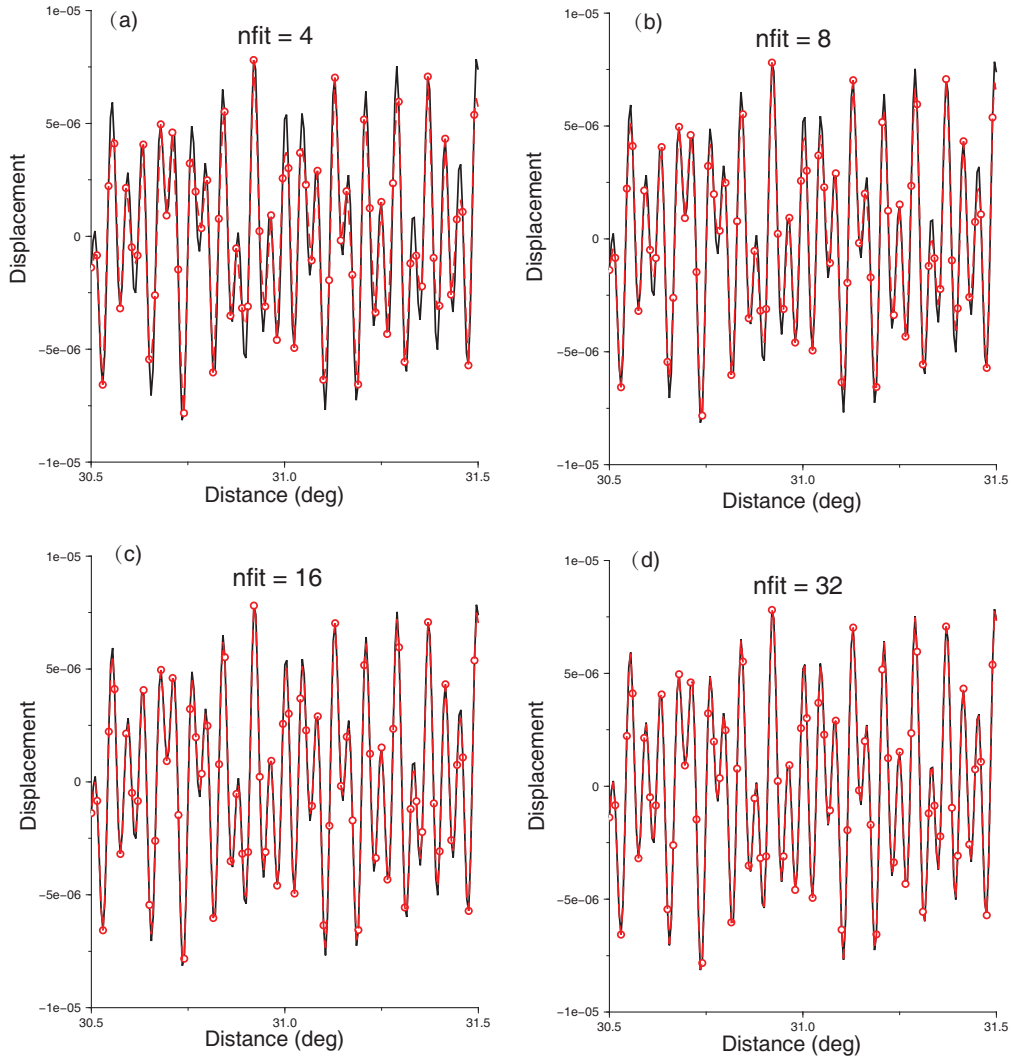

Figure S7: Testing performances of Lagrange polynomial interpolations with different degrees. The black lines are the same as Fig. S6b. "nfit" represents the degree of Lagrange polynomial. The red points with a space of 0.015^o show the values used in interpolations.

3 THE CASE OF THE 2016/10/27 M_W6.0 OFF COAST SOUTHERN CHILE EARTHQUAKE

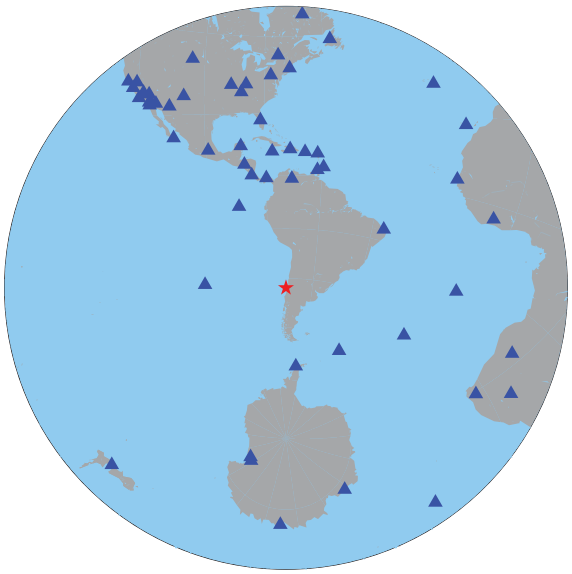

Figure S8: Teleseismic stations (blue triangles) used in Fig. 11a. The red star shows the location of earthquake.

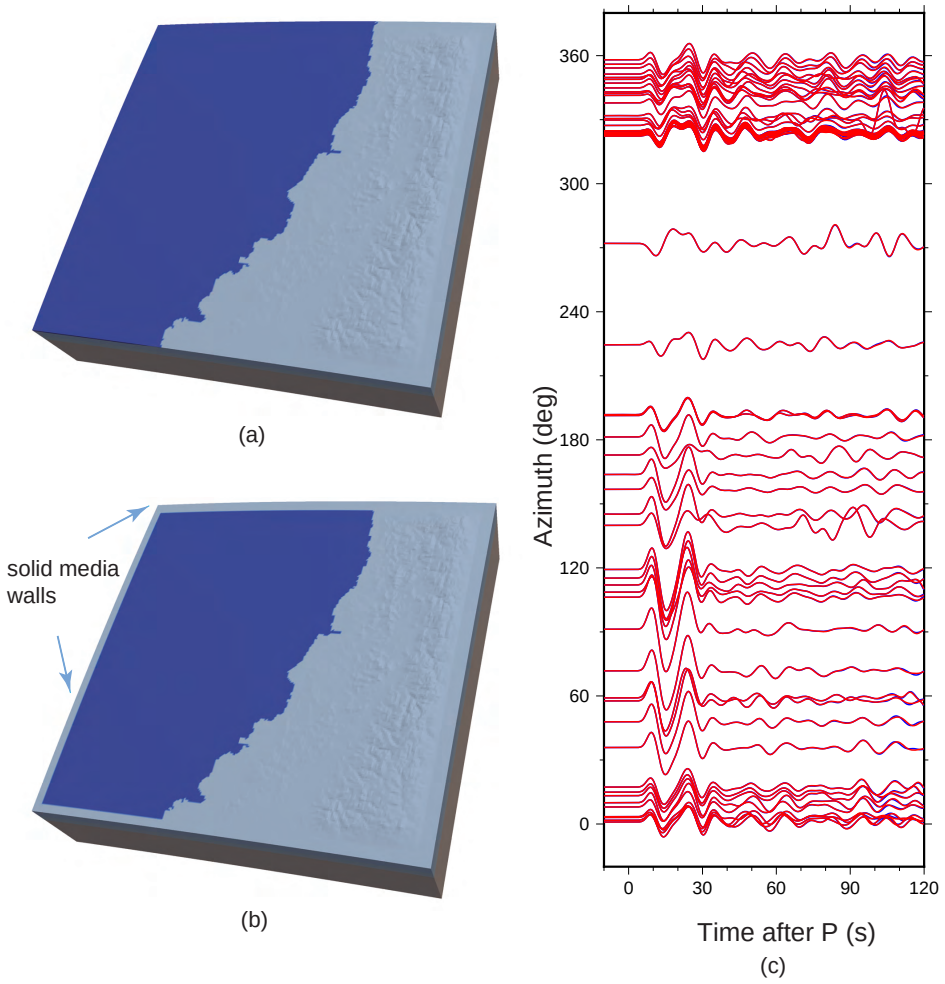

Figure S9: Testing the consequences of the mismatch between local SEM model and 1D DSM model on the coupling interface. (a) SEM model used in Fig. 12 of the main text. (b) Adding artificial solid media walls on the ocean sides of SEM box. (c) The red lines are synthetics for the model with ocean sides (Fig. S9a) and the blue lines show synthetics associated with the solid media wall model (Fig. S9b). They are pretty similar to each other and only small differences are visible in the time window 60 - 120 s.

4 STATIONS USED IN THE CASE OF THE 2009/09/10 M_W5.9 SEA OF OKHOTSK EARTHQUAKE

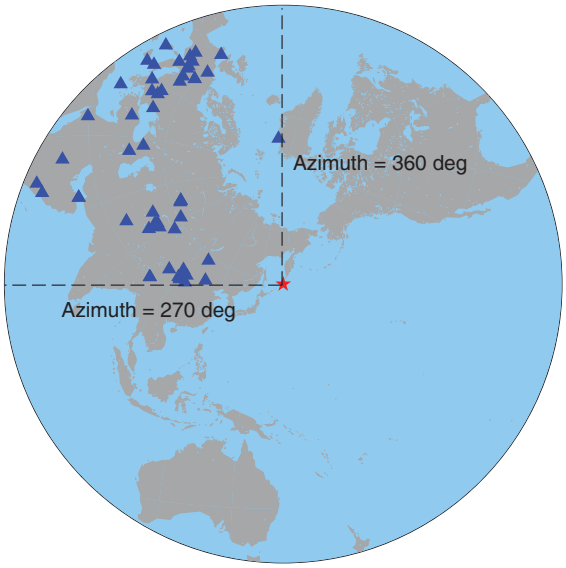

Figure S10: Stations (blue triangles) used in Fig. 14. The red star shows the location of earthquake.

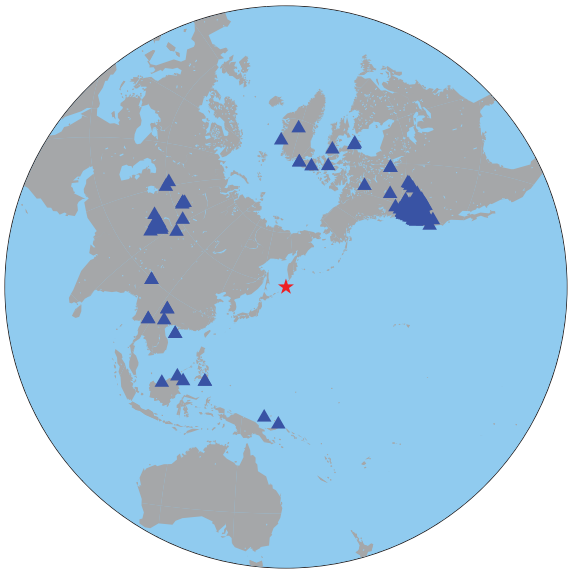

Figure S11: Stations (blue triangles) used in Fig. 15. The red star shows the location of earthquake.

REFERENCES

Abramowitz, M. & Stegun, I. A., 1964. *Handbook of mathematical functions: with formulas, graphs, and mathematical tables*, vol. 55, Courier Corporation.

Aki, K. & Richards, P. G., 2002. *Quantitative Seismology*, University Science Books, 2nd edn.

Kawai, K., Takeuchi, N., & Geller, R. J., 2006. Complete synthetic seismograms up to 2 Hz for transversely isotropic spherically symmetric media, *Geophys. J. Int.*, **164**(2), 411–424.

Skudrzyk, E., 2012. *The foundations of acoustics: basic mathematics and basic acoustics*, Springer Science & Business Media.

Zahradník, J. & Moczo, P., 1996. Hybrid seismic modeling based on discrete-wave number and finite-difference methods, *Pure appl. Geophys.*, **148**(1), 21–38.